Journal of Low Temperature Physics (2024) 216:85–93
https://doi.org/10.1007/s10909-024-03108-y

Double-Flare Angle Bowtie Slot Antenna for Multichroic CMB Polarization Detectors

Pham Viet Dung[1] · Jie Hu[1,2] · Damien Prêle[1] · Michel Piat[1]

Received: 3 November 2023 / Accepted: 1 April 2024 / Published online: 23 April 2024

Abstract

Lens antenna-coupled detectors have emerged as a prominent technology for millimeter-wave astronomy over recent decades. The future ground-based cosmic microwave background (CMB) observations that target B-modes require the receiver to operate across multiple frequency bands while maintaining effective polarization selectivity. In this context, we have reconfigured the conventional broadband bowtie slot antenna into a dual-flare angle design, exclusively targeting the CMB emission wavelength at two bands centered at 150 GHz and 220 GHz. This antenna design facilitates partial independent tuning of resonant frequencies, leading to improved impedance-matching bandwidth,that achieves a return loss of ($S_{11} < -10$ dB) spanning over an octave from 100 to 300 GHz. Simultaneously, it maintains effective linear polarization sensitivity, with cross-polarization remaining below -15 dB at both sub-bands when coupled with a dielectric lens. The integration of on-chip band-pass filters enables the effective separation of antenna signals to microwave kinetic inductance detectors. This results in a compact, polarization-selective, multichroic pixel solution that perfectly aligns with the demands of CMB B-mode observation.

Keywords Lens-coupled antenna · Double-flare angle bowtie · CMB B-mode · Multichroic detectors · MKIDs

✉ Pham Viet Dung
phamvd@apc.in2p3.fr

Jie Hu
jie.hu@obspm.fr

Damien Prêle
prele@apc.in2p3.fr

Michel Piat
piat@apc.in2p3.fr

[1] Astroparticule et Cosmologie, CNRS, Université de Paris, 10, rue Alice Domon et Léonie Duquet, 75013 Paris, France

[2] GEPI, Observatoire de Paris, CNRS, PSL Université, 77 avenue Denfert-Rochereau, 75014 Paris, France

1 Introduction

Observing the cosmic microwave background (CMB) provides profound insights into the origins and evolution of the universe [1]. However, measuring its B-mode polarization pattern remains a challenge in millimeter astronomy, mainly due to detector limitations arising from photon noise [2–4]. This emphasizes the need for next-generation telescopes featuring a significantly increased number of detectors and enhanced focal plane efficiency. Additionally, to achieve B-mode reduction polarimetry, it is imperative to observe the sky across multiple frequency bands due to foreground emissions from both galactic and extra-galactic sources [5, 6]. Antenna-coupled detectors can be designed to capture multi-frequency bands and offer polarization-selective sensitivity, particularly when integrated with on-chip band-pass filters, resulting in a compact and efficient solution for multichroic CMB detectors [7].

The bowtie slot antenna, often referred to broadband dipole or tapered slot, is preferred to couple with cryogenic detectors due to its simplicity in fabrication and broadband capabilities [8, 9]. Its planar structure not only facilitates seamless integration into various devices but also ensures consistent impedance characteristics across a broad frequency range. This makes it a compact and efficient alternative to more conventional designs like horn or sinusoidal antennas. For applications involving millimeter and sub-millimeter wave frequencies, especially in CMB observation, performance enhancements are often needed due to its limitation in impedance bandwidth. One approach is to expand the flare angle to 90 degrees [10], broadening the bandwidth at the cost of reduced polarization selectivity. Another effective approach involves employing an array configuration, such as double or dual-slot designs [11–13]. While potentially increasing the physical size, this modification can enhance frequency response, quasi-optical coupling efficiency, and overall system directivity.

This paper explores an innovative design for a bowtie slot antenna featuring a second flare angle, hence termed the double-flare angle (DFA) bowtie antenna. This design is an adaptation of the printed dipole planar bowtie antenna [14] where the flare angle is used to increase the bandwidth in dual-band operation. Our design is specifically tailored to observe CMB in multiple bands within the 100–300 GHz range, aligning with two frequency bands targeted by the CMB-S4 project [15] that are centered at 150 and 220 GHz. Additionally, the antenna must maintain sensitive linear polarization capabilities which is essential for CMB polarimetry. A compromise between various antenna aspects must be carefully considered to meet all requirements. We have limited the flare angle to a maximum of 40 degrees to ensure polarization sensitivity. Concurrently, the antenna's effective length also needs to be sufficiently compact to maintain a broad operational bandwidth while avoiding dimensions that significantly exceed the target wavelengths. Oversizing the antenna could lead to excessive standing waves, resulting in increased sidelobes, poor beam shaping, or diminished gain in the desired direction, all of which critically impact the optical coupling efficiency of the antenna.

Evaluations in this paper primarily utilize the 3D full-wave simulator—CST Studio Suite [16], complemented by Sonnet [17] for enhanced superconductor modeling accuracy.

2 Antenna design

2.1 Double-Flare Angle Bowtie

We employ a rounded-edge bowtie antenna as base geometry, originally known for its improved return loss and more stable radiation patterns [18, 19]. The conventional bowtie model is mainly defined by its length (L) and flare angle (A). The DFA configuration introduces an additional angle and length, denoted as A2 and L2 (with the geometry constraint $L2 < L1$ and $A2 > A1$). The primary flare angle A and length L are then denoted as A1 and L1, as shown in Fig. 1a.

Our analysis commenced by examining the antenna input impedance (Z_{11}) using Transient solver in CST. The simulation model and result are depicted in Fig. 1. A lumped discrete port (depicted as a red cone) feeds the antenna at the center, with the port's impedance (Z_0) arbitrarily chosen. The Z_{11} is the antenna's inherent property driven by its geometry and is independent of the input port impedance Z_0. The antenna return loss (S_{11}) response, however, can vary widely depending on Z_0 and is easily obtained with the following relationship: $S_{11} = \frac{Z_{11}-Z_0}{Z_{11}+Z_0}$.

The parametric simulations of the traditional bowtie, as shown in Fig. 2a, b, reveal that the angle A is the primary determinant of the antenna's bandwidth. Increasing A maintains the first resonance point while flattening the real part of Z_{11}, thus broadening the impedance bandwidth. On the other hand, the length L mainly influences the resonant frequency of the bowtie by shifting the entire Z_{11} curve. The simulated behaviors of A and L therefore are consistent with theoretical expectations [20].

In the case of the DFA bowtie, illustrated in Fig.2c, d, adjustments to length L2 result in minor shifts in the imaginary part of Z_{11} and a decrease in resistance at the second resonance point when L2 is increased. If L2 approaches L1, the DFA bowtie

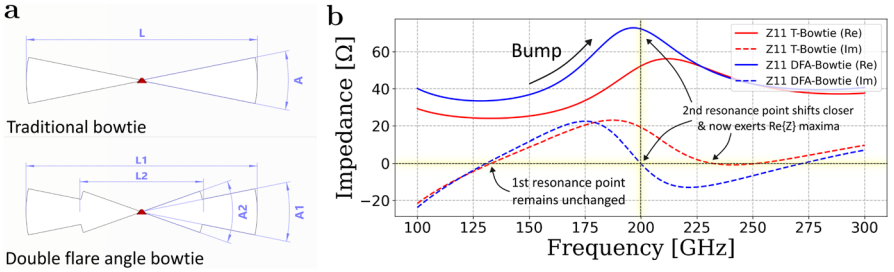

Fig. 1 **a** Parametric designs of traditional (T-Bowtie) and double-flare angle (DFA-Bowtie) antennas. **b** Z_{11} comparison illustrates the additional flare angle bringing the second resonant frequency point nearer to the first one, enabling the second resonant frequency tuning feature but also increasing the overall resistivity of the antenna

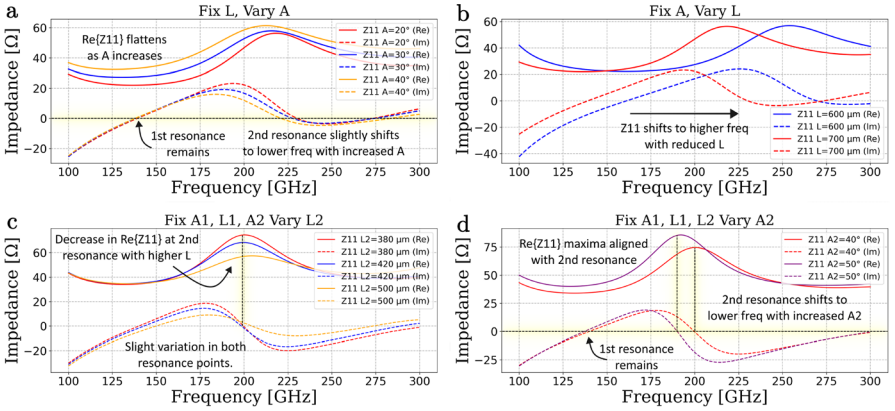

Fig. 2 Parametric study of antenna input impedance Z_{11}. **a**, **b**: L and A of T-Bowtie; **c**, **d**: L2 and A2 of DFA-Bowtie

transitions back to a traditional configuration, contradicting the DFA's geometric constraints. Expanding angle A2 predominantly impacts the second resonance frequency, pulling it closer and increasing the overall resistive component of the antenna.

In general, despite the impacts of these parameters on the impedance profile of the DFA as we tested, the characteristic shape of S_{11} remains unchanged, that is, there are always 2 points of resonant frequency and the real part (resistance) of these two points is always different. Therefore, unless being fed by two different impedances correspondingly, this antenna can never achieve multi-band operation because there will always be impedance mismatch in each sub-band.

2.2 Optimization

Our primary objective is to design the antenna for dual sub-band operation, specifically targeting 150 GHz and 220 GHz with a 20% bandwidth for each band. To ideally achieve this, we aim for Z_{11} to be purely resistive (zero reactance) at both frequencies, and their values must be equal to facilitate multi-band operation with a single-input impedance, i.e., one feedline. Essentially, the antenna must satisfy the following two conditions simultaneously:

$$\mathrm{Re}\{Z_{11}\}|_{f=150\,\mathrm{GHz}} = \mathrm{Re}\{Z_{11}\}|_{f=220\,\mathrm{GHz}}, \tag{1}$$

$$\mathrm{Im}\{Z_{11}\}|_{f=150\,\mathrm{GHz}} = \mathrm{Im}\{Z_{11}\}|_{f=220\,\mathrm{GHz}} = 0. \tag{2}$$

As studied in section , meeting these criteria at the same time is challenging for the DFA design due to its inherent planar physical limitations and the natural frequency-dependent behavior of reactance. Our strategy involves optimizing each condition independently and then finding an optimal balance between them. The final

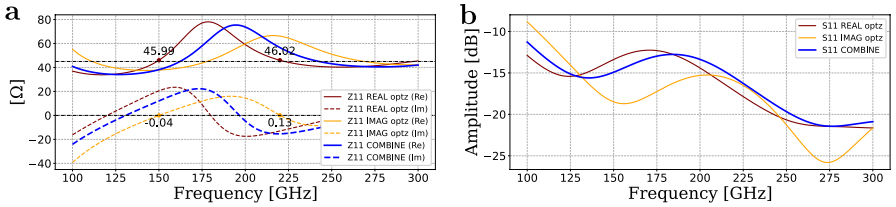

Fig. 3 **a** Optimization scheme for Z_{11} and **b** corresponding S_{11} obtained at Z_0 chosen to be 48Ω. The orange curve zeroes the imaginary part at 150 and 220 GHz; the brown curve aligns the real part with 46 Ω at both frequencies. The blue curve represents the average of these two, constituting the final optimization result. This result is adopted for our DFA-Bowtie configuration, with detailed values provided in Table 1

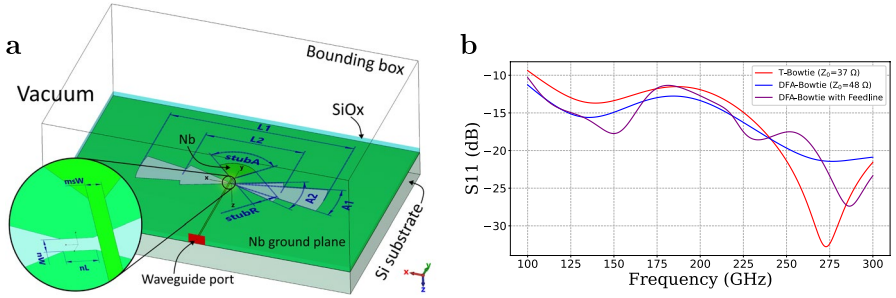

Fig. 4 **a** Parametric design and model stratification in CST. **b** Antenna return loss (S_{11}) comparison between T-Bowtie, DFA-Bowtie, and DFA-Bowtie with feedline

optimization is represented by the blue curves in Fig. 3, focusing on the adjustment of parameters A1, L1, A2, and L2.

2.3 Microstrip Feedline Integration

The finalized antenna model, depicted in Fig. 4a, features a slot antenna etched into a niobium ground plane on a silicon substrate. This antenna is fed via a microstrip feedline, separated by an 885-nm-thick SiO_x dielectric layer with a relative permittivity of $\epsilon_r = 4.318$ ([21, 22]). The feedline terminates by a radial stub that provides wideband impedance matching and exhibits a virtual short circuit to the ground [23, 24]. The radial stub's dimensions, including radius (*stubR*), angle (*stubA*), and position (*stubH*), are finely tuned to facilitate complete broadband frequency transfer from the feedline to the antenna. The feedline, composed of niobium like the ground plane, exhibits a surface impedance of 0.2 pH/□ in cryogenic state. The simulations are conducted using the CST frequency domain solver, taking into account the niobium kinetic inductance effect. Notably, the use of CST is crucial to ensure alignment with Sonnet for precise 3D superconducting antenna simulations [25].

Table 1 Parametric values

T-Bowtie	DFA-Bowtie	Feedline
A = 23°	A1 = 23, A2 = 40°	stubA = 90°
L = 720μm	L1 = 720, L2 = 385μm	stubR = 100μm
nL = 10μm	nL = 10μm	stubH = 1μm
nW = 4μm	nW = 4μm	msW = 2.5μm

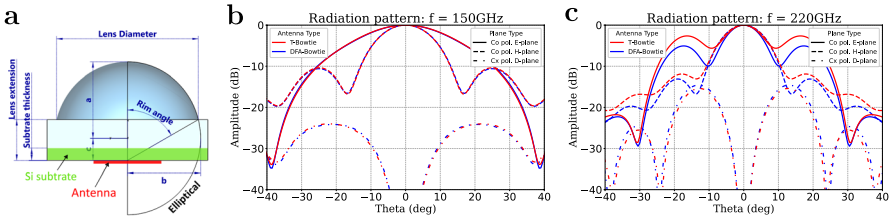

Fig. 5 **a** Silicon elliptical lens schematic with slot antenna positioned at its second focus. **b**, **c** Comparison of radiation pattern for both bowtie designs at 150 and 220 GHz

The microstrip line width (msW) is fine-tuned using Sonnet to achieve a characteristic impedance of approximately 48 Ω. This impedance matches the port impedance Z_0 that was employed in our previous optimization to yield the optimal S_{11}. Realizing high impedances on a microstrip line is difficult, as it necessitates reducing the width of the trace to a point where it becomes highly sensitive to fabrication tolerances. The optimal value of msW is determined from simulation to be 2.5 μm, which is at the threshold of our current fabrication we have.

As shown in Fig. 4b, the S_{11} obtained from the feedline model aligns well with the optimized S_{11} achieved from Fig. 3b, thereby validating our design approach. It is remarkably revealed that a conventional bowtie antenna, defined by dimensions $A = A1$ and $L = L1$ and without the additional flare angles A2 and L2, can also attain an $S_{11} < -10dB$ across an octave band. This performance is merely achievable when the antenna operates at an appropriate impedance of $Z_0 = 37$ Ω These comparisons underscore the marginally enhanced performance reliability of the DFA-Bowtie design compared to its traditional counterpart.

3 Antenna-Lens Coupling

3.1 Lens Design and Integration

The antenna is positioned at the second foci of a silicon elliptical lens, as shown in Fig. 5a, to improve its gain and directivity. Silicon ($\varepsilon_r = 11.9$) is the preferred lens material for its low-loss properties at millimeter and sub-millimeter wavelengths [26]. Following the designs in [27, 28], the simulated lens has a 6 mm diameter—approximately triple the wavelength of the central bandwidth—and features a rim

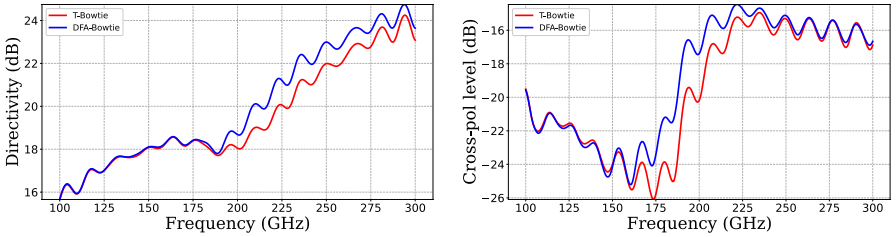

Fig. 6 Comparison of directivity and cross-polarization levels for both bowtie designs

angle of 70°. The semi-major axis and semi-minor axis of the elliptical lens are $a = 3.140$mm and $b = 3.005$mm.

3.2 Performance and Results

We compared the radiation pattern of the DFA and the traditional bowie with CST at 150 and 220 GHz, as is shown in Fig. 5b, c. It can be seen that the radiation patterns are identical at 150 GHz due to the DFA and traditional bowtie sharing the same first flare angle and length. However, at 220 GHz, the DFA demonstrates a notable side-lobe reduction of several dB. This improvement suggests a potential for further side-lobe reduction by optimizing the shape of the dielectric lens.

The cross-polarization across the operation bandwidth is shown in Fig. 6. It shows the lens-coupled DFA maintains a cross-polarization level below −15 dB across the band simulated and is comparable with the traditional bowtie, which means there is no degradation by introducing the second flare in the design. In general, the cross-polarization becomes higher as frequencies increase. This tendency is due to the current distribution on the antenna surface, which determines its radiation pattern and polarization characteristics [19]. As the antenna becomes electrically large relative to shorter wavelengths, the potential for multiple radiation modes increases, elevating cross-polarization levels.

4 Conclusion and Perspective

In this study, we have proposed an innovative bowtie slot antenna design that is specifically optimized for CMB B-mode detectors, which demonstrates a performance slightly superior to that of a conventional one. Our latest simulations indicate a $S_{11} < -10$ dB and cross-polarization less than −15 dB across a wide range of frequencies from 100 to 300 GHz. Further optimization of the far-field performance, including aspects such as sidelobe and Gaussian coupling efficiency, is in progress. This antenna is intended to be used as the receiving element in a dual-color multichroic CMB detector employing MKIDs. Next step will be to fabricate and test this design by the end of the year, aiming to assess its effectiveness for CMB B-mode polarimetry and to guide further improvements.

Acknowledgements The authors express their gratitude to Steve Torchinsky and Manuel Gonzalez for their valuable discussions and revision of this paper. Special thanks to the prestigious "France Excellence" 2021 Scholarship program of the French Embassy in Vietnam for supporting this research work.

References

1. S. Staggs, J. Dunkley, L. Page, Recent discoveries from the cosmic microwave background: a review of recent progress. Rep. Prog. Phys. **81**(4), 044901 (2018). https://doi.org/10.1088/1361-6633/aa94d5
2. C.A. Hill, A. Kusaka, Photon noise correlations in millimeter-wave telescopes (2023)
3. I.J. Agulo, L. Kuzmin, Responsivity and noise equivalent power of a single cold-electron bolometer. Appl. Sci. **11**(10) (2021) https://doi.org/10.3390/app11104608
4. G. Pascual-Cisneros, F.J. Casas, P. Vielva, Optimization of a microwave polarimeter for astronomy with optical correlation and detection. Sensors **23**(5), (2023) https://doi.org/10.3390/s23052414
5. M. Tegmark, D.J. Eisenstein, W. Hu, A. Oliveira-Costa, Foregrounds and forecasts for the cosmic microwave background. Astrophys. J. **530**(1), 133–165 (2000). https://doi.org/10.1086/308348
6. L. Knox, Forecasting foreground impact on cosmic microwave background measurements. Monthly Notices R. Astronom. Soc. **307**(4), 977–983 (1999) https://doi.org/10.1046/j.1365-8711.1999.02687.xhttps://academic.oup.com/mnras/article-pdf/307/4/977/18637659/307-4-977.pdf
7. A. Traini, A. Tartari, G. Bordier, et al, Dual-color antenna-coupled lekid for next-generation multi-chroic cmb focal planes. J. Low. Temp. Phys. **193**, 170–175 (2018) https://doi.org/10.1007/s10909-018-2038-5
8. S. Hähnle, O. Yurduseven, S. Berkel, N. Llombart, J. Bueno, S.J.C. Yates, V. Murugesan, D.J. Thoen, A. Neto, J.J.A. Baselmans, An ultrawideband leaky lens antenna for broadband spectroscopic imaging applications. IEEE Trans. Antennas Propag.**68**(7), 5675–5679 (2020). https://doi.org/10.1109/TAP.2019.2963563
9. J. Bueno, V. Murugesan, K. Karatsu, et al, Ultrasensitive kilo-pixel imaging array of photon noise-limited kinetic inductance detectors over an octave of bandwidth for thz astronomy. J. Low Temp. Phys. **193**, 96–102 (2018) https://doi.org/10.1007/s10909-018-1962-8
10. J. J. A. Baselmans, F. Facchin, A. Pascual Laguna, J. Bueno, D. J. Thoen, V. Murugesan, N. Llombart, P. J. de Visser, Ultra-sensitive thz microwave kinetic inductance detectors for future space telescopes. A&A **665**, 17 (2022) https://doi.org/10.1051/0004-6361/202243840
11. A.J. Alazemi, H.-H. Yang, G.M. Rebeiz, Double bow-tie slot antennas for wideband millimeter-wave and terahertz applications. IEEE Trans. Terahertz Sci. Technol. **6**(5), 682–689 (2016). https://doi.org/10.1109/TTHZ.2016.2590947
12. J. Wheeler, S. Hailey-Dunsheath, E. Shirokoff, et al, Superspec, the on-chip spectrometer: Improved nep and antenna performance. J. Low Temp. Phys. 193, 408–414 (2018) https://doi.org/10.1007/s10909-018-1926-z
13. S. Berkel, E.S. Malotaux, C. De Martino, M. Spirito, D. Cavallo, A. Neto, N. Llombart, Wideband double leaky slot lens antennas in cmos technology at submillimeter wavelengths. IEEE Trans. Terahertz Sci. Technol. **10**(5), 540–553 (2020). https://doi.org/10.1109/TTHZ.2020.3006750
14. H. Andre, R. Fernandez, Baharuddin: Dipole planar bowtie printed antenna for ism application. IOP Conf. Ser. Mater. Sci. Eng. **602**(1), 012022 (2019). https://doi.org/10.1088/1757-899X/602/1/012022
15. K.N. Abazajian, P. Adshead, Z. Ahmed, et al, CMB-S4 Science Book, First Edition (2016). arXiv:1610.02743v1
16. Dassault Systèmes, CST Studio Suite (2023). https://www.3ds.com/products-services/simulia/products/cst-studio-suite/
17. Sonnet Software, IC and Chip Design (2023). https://www.sonnetsoftware.com/
18. S.-W. Qu, C. Ruan, Effect of round corners on bowtie antennas. Progress in Electromagnetics Research-pier - PROG ELECTROMAGN RES 57, 179–195 (2006) https://doi.org/10.2528/PIER05072103
19. R. Mello, A. Lepage, X. Begaud, The bow–tie antenna: performance limitations and improvements. IET Microwaves, Antennas Propag. **16** (2022) https://doi.org/10.1049/mia2.12242
20. C.A. Balanis, *Antenna Theory: Analysis and Design*, 4th edn. (John wiley & Sons, New York, 2016)

21. R. Datta, The first multichroic receiver and results from actpol. PhD thesis (January 2016)
22. A. Neto, D. Bekers, G. Gerini, J. Baselmans, S. Yates, H. Hoevers, Ebg enhanced dielectric lens antennas for the imaging at sub-mm waves. In: 2008 IEEE Antennas and Propagation Society International Symposium, pp. 1–4 (2008). https://doi.org/10.1109/APS.2008.4619323
23. D. Cavallo, W. Syed, A. Neto, A 5:1 connected slot array loaded with artificial dielectric layers, pp. 1–4 (2016). https://doi.org/10.1109/ARRAY.2016.7832629
24. M.M. Zinieris, R. Sloan, L.E. Davis, A broadband microstrip-to-slot-line transition. Microwave Opt. Technol. Lett. **18**(5), 339–342 (1998). https://doi.org/10.1002/(SICI)1098-2760(19980805)18:5<339::AID-MOP9>3.0.CO;2-9
25. A. Endo, A. Pascual Laguna, S. Hähnle, K. Karatsu, D.J. Thoen, V. Murugesan, J.J.A. Baselmans, Simulating the radiation loss of superconducting submillimeter wave filters and transmission lines using Sonnet EM. J. Astronom. Telescopes Instruments Syst. **8**, 036005 (2022) https://doi.org/10.1117/1.JATIS.8.3.036005
26. L. Ferrari, O. Yurduseven, N. Llombart, S.J.C. Yates, J. Bueno, V. Murugesan, D.J. Thoen, A. Endo, A.M. Baryshev, J.J.A. Baselmans, Antenna coupled mkid performance verification at 850 ghz for large format astrophysics arrays. IEEE Trans. Terahertz Sci. Technol. **8**(1), 127–139 (2018). https://doi.org/10.1109/TTHZ.2017.2764378
27. D.F. Filipovic, S.S. Gearhart, G.M. Rebeiz, Double-slot antennas on extended hemispherical and elliptical silicon dielectric lenses. IEEE Trans. Microwave Theory Tech. **41**(10), 1738–1749 (1993). https://doi.org/10.1109/22.247919
28. H. Zhang, S.O. Dabironezare, G. Carluccio, A. Neto, N. Llombart, A go/fo tool for analyzing quasi-optical systems in reception. In: 2019 44th International Conference on Infrared, Millimeter, and Terahertz Waves (IRMMW-THz), pp. 1–2 (2019). https://doi.org/10.1109/IRMMW-THz.2019.8873950